PAPER • OPEN ACCESS

Calibration methodology for contact heat flux sensors with enhanced accuracy

View the article online for updates and enhancements.

Calibration methodology for contact heat flux sensors with enhanced accuracy

G Rizzo , R Christen and M Stöck

Institute for Development of Mechatronic Systems, OST Eastern Switzerland University of Applied Sciences, Werdenbergstrasse 4, Buchs CH-9471, Switzerland

E-mail: gerhard.rizzo@ost.ch

CrossMark

Abstract

This paper presents a method for the calibration of contact heat flow sensors and the measures taken to improve the overall standard uncertainty of the measurements. This may be particularly relevant for applications such as the thermal characterization of Li-ion battery cells, where small amounts of transferred heat must be measured. The designed calibration set-up is based on the measurement of temperature gradients within a reference object, which is a common and well known approach. However, certain aspects must be considered in order to obtain accurate results. In this paper all steps taken to improve the overall measurement uncertainty are described. One of the most important characteristics of the presented methodology is the experimental determination of an equivalent thermal conductivity of the used reference object. To do so, a single-sided guarded hot plate apparatus is integrated into the calibration set-up to generate a precisely known heat flow. This approach is comparable to the determination of the 'energy equivalent' in calorimeters. The measured equivalent thermal conductivity agrees well to literature values, but the achieved standard uncertainty is significantly lower. By way of example, the calibration method is applied on a thermoelectric generator, where the temperature dependent sensitivity and the Seebeck coefficient are determined and compared to literature values. The average standard uncertainty of the sensor sensitivity is $\pm 1.86\%$, which is lower than most results published in the literature. At $20\,^\circ$C the absolute value of the determined Seebeck coefficient of the examined thermoelectric element is only 2.7% higher than the value expected for the used material (Bi_2Te_3).

Keywords: heat flux sensor, Peltier-element, calibration, measurement uncertainty, thermal conductivity

(Some figures may appear in colour only in the online journal)

1. Introduction

Quantitative measurement of the exact amount of transferred heat is an essential analysis method in many natural scientific and engineering fields as well as in production and quality control [1]. Especially in the field of Li-Ion battery testing, the measurement of heat flux has become an important tool to determine the thermal behavior of battery cells and thus enabling an accurate modeling [2, 3]. In such applications, high requirements are posed on the sensor with regard to its accuracy, since the heat flux to be measured is often in the range of only a few hundred $W\,m^{-2}$. In general, the importance of accurate calibration of heat flow sensors has already

been pointed out by Childs *et al* [4]. For the applications considered in this paper the sensor does not require a large range of operating temperature, as Li-Ion cells can neither be used at very high nor very low temperatures. These specific requirements are not limited to the field of battery testing but apply also to other areas, such as power dissipation measurements in power electronics [5] or investigations on bacteria growth in microbiology [6, 7]. Most of the literature, in which the properties of thermoelectric generators (TEG) are examined, deals with the determination of the Seebeck coefficient under extreme conditions such as high temperature [8, 9] or large temperature ranges [10, 11]. However, if a TEG shall be used to measure the heat flux, the needed quantity for the calibration process is the effective heat flux instead of the temperature difference across the TEG. Therefore an adequate calibration set-up with the ability to precisely determine the present heat flux has to be designed. For the sake of completeness, it shall be mentioned that for heat flux sensors that are used to control a zero heat flow, the sensitivity accuracy is not of importance [12].

Heat appears exclusively during the transfer of thermal energy from one system to another. The driving force for heat exchange is the temperature gradient ∇T between these systems. The steeper the gradient the higher the heat exchange rate, i.e. the greater the amount of heat transmitted per unit of time, or heat flow [1]. However, heat exchange also occurs inside of materials. Theoretically, an infinite number of single systems can discretize any continuum [13]. Fourier's law of thermal conduction

$$\vec{\dot{q}} = -k \cdot \nabla T, \tag{1}$$

which describes the linear relationship between the spatial temperature gradient and the heat flux, is valid for solid materials. Thereby, the heat flux $\vec{\dot{q}}$ represents the amount of heat that is transferred per time through a defined isothermal surface, whereas k denotes the thermal conductivity of the solid material. This corresponds to the above-mentioned heat flow divided by the transfer surface [14].

Unfortunately, neither heat flux nor heat flow can be measured directly, since only the effects caused by the transferred heat can be detected [1]. In principal, there are three such effects of a heat exchange:

(a) Heating up or cooling down of a substance, i.e. a change in temperature can be observed.
(b) Melting, evaporation or sublimation of a substance, in which case heat is transferred to the substance. If heat is removed, the substance will freeze, condensate or resublimate, respectively.
(c) Occurrence of a temperature gradient along the heat transfer path within a solid.

The first two effects listed above are used in calorimeters, since the absolute amount of heat exchanged is of interest in these applications. If the amount of heat transferred per unit of

time through a defined area is to be measured, the third effect mentioned above can be used. According to equation (1), both the temperature gradient and the thermal conductivity of the reference object must be known precisely in order to calculate the causing heat flow.

Nowadays, the temperature gradient can be measured with high precision if appropriate precautions are taken regarding sensor positioning and accuracy. Additionally, if the error propagation is applied to the linear regression [15], it was found that the uncertainty of the temperature gradient is greatly affected by the uncertainties of the underlying data sets. If the thermal conductivity of the reference material is obtained from a data sheet of the material manufacturer or is determined with reference measurements in an independent laboratory, there are two major disadvantages. Firstly, the uncertainty of the thermal conductivity is not necessarily available in a data sheet, leading to missing information when calculating the error propagation. Secondly, the heat flow disturbances in the reference object introduced due to sensor placement are not taken into account. This can lead to significant errors in the calculation of the heat flux used for the calibration of the sensor. In order to reduce the influence of uncertain material properties, this paper presents a methodology that uses the same set-up for the determination of the equivalent thermal conductivity of the reference object, as well as for the calibration of the heat flux sensor. Thereby, the existing disturbances of the temperature field in the reference object are taken into account, which improves the accuracy of the sensor calibration. In addition, the then known uncertainty of the equivalent thermal conductivity value is taken into consideration by a rigorous application of the law of error propagation for both directly calculated quantities and linear regression coefficients. This methodology leads ultimately to the overall uncertainty of the sensor sensitivity.

2. Materials and methods

Assuming a known one-dimensional heat flow $\dot{q}_{\text{provoked}}$ is imposed along a reference object and the resulting temperature gradient $\frac{\partial \vartheta}{\partial x}$ is measured, the thermal conductivity k of the material can be calculated according to equation (1).

$$k = -\frac{\dot{q}_{\text{provoked}}}{\frac{\partial \vartheta}{\partial x}}. \tag{2}$$

Once the material property k is no longer unknown, equation (1) can also be used to calculate the prevailing heat flux from the measured temperature gradient for the one-dimensional case.

$$\dot{q} = -k \cdot \frac{\partial \vartheta}{\partial x}. \tag{3}$$

To calibrate a heat flux sensor, it is placed on top of the reference object to form a thermal series connection. Assuming that radial heat losses to the environment can be neglected,

the total amount of heat entering the top side of the sensor will flow through the sensor and the reference object towards the constant sink temperature. To ensure this, the sensor and the reference object have to be insulated and the surroundings must be kept at a constant temperature level throughout the entire experiment. In addition, heat losses via wires—for example the signal lines used for temperature measurement—have to be minimized. Hence, the diameter is chosen to be as small as possible and the wires are routed radially on a preferably isothermal path. Figure 1 shows a schematic cross-section of the designed calibration set-up for heat flux sensors in an assembled state, as used in this investigation. All hatched parts represent the actual calibration setup, while the remaining parts represent the heat flux sensor to be calibrated, which is also shown as a close-up in figure 1. The set-up used consists of a temperature-controlled aluminum enclosure, which guarantees a defined ambient condition during the experiment and shields the reference object from external temperature fluctuations. For this purpose, cooling channels were integrated into the enclosure through which a coolant is circulated. The temperature ϑ_{sur} of the coolant and hence the surrounding enclosure is controlled by means of a Ministat 125 cryostat from Peter Huber Kältemaschinenbau AG. The reference object placed in the center of the enclosure is an AISI 304 grade stainless steel bar with a length of 50 mm and a square cross-section of $A = (L_{ro})^2$, and an edge length of $L_{ro} = (17.000 \pm 0.058)$ mm. The reference object is force-fitted into the bottom of the enclosure, which also serves as a heat sink. The cavity between the reference object and the enclosure is filled with insulating foam, shown in light yellow in figure 1, to minimize heat losses in a radial direction. The thermal conductivity of the swissporXPS Premium Plus 300 GE insulation foam used is less than $0.027\,\mathrm{W\,(m\,K)^{-1}}$ according to the manufacturer's specifications.

The heat flux sensor to be calibrated is coaxially aligned and placed on top of the reference object. In order to generate the necessary heat flux for calibration of the sensor, a heating and/or cooling device is needed on the top side of the sensor. Hence, the heat generated flows through the sensor and the reference object toward the temperature-controlled enclosure. As an application example, the calibration method introduced in this paper is applied on a combined temperature/heat flux sensor (THFS) used for the experimental characterization of the thermal behavior of Lithium ion battery cells [16]. The close-up in figure 1 depicts the layered structure of the THFS. It consists of a copper front plate with an integrated thermocouple to measure surface temperature, a TEG, which is the actual heat flux sensor [17], and a thermoelectric cooler (TEC), which serves as an active cooling or heating unit. The copper plate, the TEG and the TEC have the same square area of 15 mm × 15 mm. They are glued together with an highly heat conductive adhesive, so that the thermal contact resistance between these three parts can be neglected, especially with the low heat flux applied in this work. Detailed information on modes of operation and the application can be found in [16]. However, the presented calibration methodology and

the experimental set-up are not limited to this type of heat flux sensor. Any type of heat flux sensor with the same active measuring area can be installed, in which case an additional heating/cooling device must also be installed. In case sensors with a different measuring area need to be calibrated, also the geometry of the reference object must be adapted accordingly. However, it was not investigated if the presented methodology is also applicable to micro-scale heat flux sensors.

2.1. Measurement of temperature gradients

In order to determine the temperature gradient $\partial\vartheta/\partial x$ along the height of the reference object, the temperature is measured at five distinct positions. For this purpose resistance temperature detectors (RTD) of type 3911 and an accuracy class 1/10 DIN are used. These RTD have an outer diameter of 1.2 mm and a length of 15 mm. According to the RTD manufacturer, a helix made of a platinum wire is placed inside the ceramic tube, with the remaining air gaps being filled with an aluminum oxide powder. The thermal conductivity of the RTD material is in the range of 20–$30\,\mathrm{W\,(m\,K)^{-1}}$, which is comparable to the property of the surrounding stainless steel. As shown in figure 1, the sensors are placed in boreholes perpendicular to the longitudinal axis of the cuboid. The exact positions of the borehole centers relative to the upper edge of the reference object, as shown in table 1, were determined using coordinate measuring technology. Thereby, an average borehole diameter of (1.3691 ± 0.0021) mm was measured. The RTD probes posses a slightly smaller diameter of (1.1942 ± 0.0052) mm, as measured with a calibrated micrometer gauge. Therefore, it can be stated with a confidence interval of 95% that the sensor position will fall into the interval of ± 0.1 mm around the borehole center. Assuming a uniform probability distribution the standard uncertainty of the sensor position follows to be $0.1\,\mathrm{mm}/\sqrt{3} = 0.058$ mm. However, it should be noted that due to the physical dimensions of the platinum helix, the RTD measures an average temperature over the entire volume of the sensor. Data acquisition is performed with a PXIe-System from National Instruments (NI). The RTD are connected to the PXIe-4357 measurement card by a 4 wire scheme. To minimize possible heat transfer via the signal lines, thin copper wires with a cross-sectional area of only $0.14\,\mathrm{mm^2}$ are used.

Before installing the RTD in the boreholes of the reference object, the relative gain and offset deviations of all used RTD were determined and compared to tolerance in the class 1/10 DIN, which is as small as $\pm(0.03\,^\circ\mathrm{C} + 0.0005 \cdot \vartheta_m)$, where ϑ_m is the measured value in $^\circ$C. For this purpose, the sensors were symmetrically placed into a copper block and measurements were taken at various stationary temperature levels. The data was compared with the measured average temperature, which allowed the relative gain and offset variation to be calculated. In table 1, the values for the found gain and offset variation are listed together with the exact sensor location along the axis of the reference object. As shown, the offsets of all examined
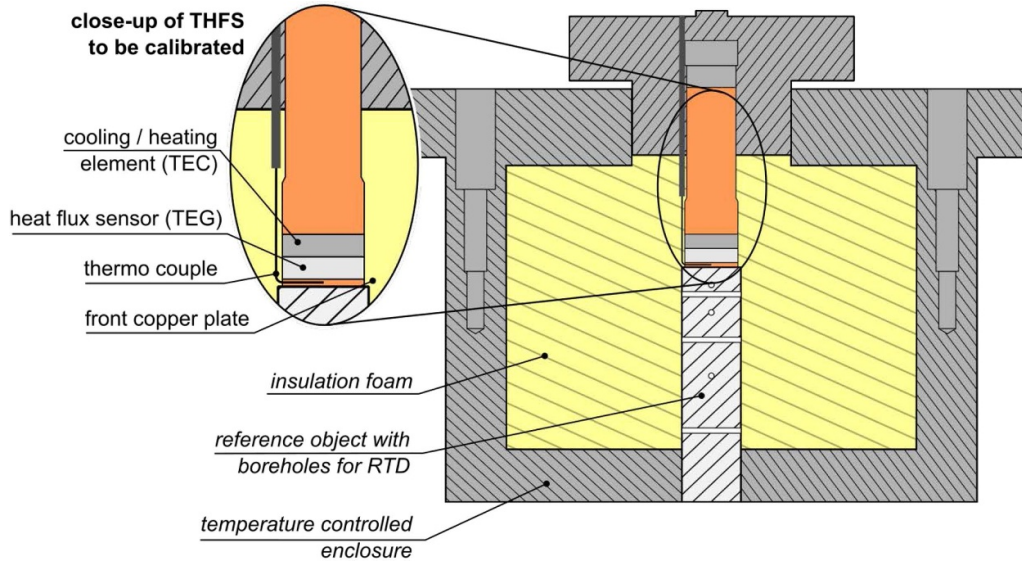
Figure 1. Schematic cross section of the heat flux calibration set-up.

Table 1. Position of the RTD sensors (type 3911—class 1/10 DIN). The position $x = 0$ mm corresponds to the top side of the reference object. Additionally, the determined gain and offset deviations are listed.

Sensor position x	Gain	Offset
(7.218 ± 0.058) mm	1.000 00	4.9 mK
(12.240 ± 0.058) mm	1.000 10	10.8 mK
(19.761 ± 0.058) mm	0.999 37	-21.9 mK
(29.728 ± 0.058) mm	1.000 12	-5.3 mK
(44.795 ± 0.058) mm	1.000 20	14.7 mK

temperature sensors are actually within the specified tolerance of the accuracy class 1/10 DIN.

Another important requirement to apply equations (2), (3) on a macroscopic level is the attainment of a steady state. In this paper it is assumed, that the temperature gradient can be considered as stationary if none of the temperatures measured along the reference object change by more than 5 mK during a time interval of 5 min. After the steady state is reached, all temperatures ϑ_i are measured and plotted against the sensor positions x_i. A linear regression model of the following type can be applied:

$$\hat{\vartheta}_i = \vartheta_i - \epsilon_i = \beta_0 + \beta_1 \cdot x_i \qquad (4)$$

where ϑ_i and x_i are the measured values, $\hat{\vartheta}_i$ are the estimated values and ε_i are the related residuals. In this example, the coefficient β_1 corresponds to the temperature gradient $\partial\vartheta/\partial x$. As stated in [15], the standard deviation of such a regression model is often used as a measure for the uncertainty of the coefficients found. However, the empirical standard deviation is in fact only a measure of the quality of the regression, i.e. how well the relationship between two quantities can be expressed by a linear model. In order to account for the

uncertainties of the two underlying data sets, the law of error propagation has to be applied. Explicit formulas considering this were presented by Matus [15], which are consistent with the guide to the expression of uncertainty in measurement (GUM) [18]. The equations given in appendix A are applied each time a linear regression is used.

2.2. Thermal conductivity of the reference object

Before calibration of the heat flux sensors can be performed, the equivalent thermal conductivity of the reference object has to be determined and verified. As mentioned above, this step is only performed after the reference object, with the existing boreholes and the fitted RTD, has been installed in the calibration setup in its final position. This approach yields a double advantage. On the one hand, the equivalent thermal conductivity of the reference object takes into account the existing irregularities in the supposedly uniaxial temperature distribution, which are caused by the design of the calibration setup itself. On the other hand, the subsequent calculation of the error propagation does not have to consider additional uncertainties of the material property. To do so, the single-sided guarded hot plate (1S-GHP) method [19] was used to generate a known heat flow within the reference object, so that the occurring temperature gradient could be measured. Subsequently, the equivalent thermal conductivity was calculated with equation (2). The applied method and its implementation is described in more detail in appendix C. Due to the fact that the thermal conductivity of the stainless steel used is temperature dependent [20], the value has to be determined for different temperature levels. This was accomplished by keeping the bottom side of the reference object at a constant temperature of $\vartheta_{sur} = 18\,°C$, while the heating power $\dot{Q}_{el}$ of the 1S-GHP on the top side was increased in several steps. It is assumed

that the amount of heat which is not conducted into the reference object is negligible due to the applied 1S-GHP method. Therefore, the heat flux can be expressed according to:

$$\dot{q} = \frac{\dot{Q}_{\text{el}}}{(L_{\text{ro}})^2} = \frac{U \cdot I}{(L_{\text{ro}})^2}, \tag{5}$$

where U is the voltage drop across the resistive heating element, I is the applied electrical current and L_{ro} is the edge length of the reference object. According to the law of error propagation the associated measurement uncertainty of the heat flux can be expressed by:

$$u^2(\dot{q}) = \left[\frac{\partial \dot{q}}{\partial I} \cdot u(I)\right]^2 + \left[\frac{\partial \dot{q}}{\partial U} \cdot u(U)\right]^2 + \left[\frac{\partial \dot{q}}{\partial L_{\text{ro}}} \cdot u(L_{\text{ro}})\right]^2. \tag{6}$$

Finally, each thermal conductivity value k_m—calculated using equation (2)—is assigned to the corresponding average temperature ϑ_m of the reference object for the respective experiment. This is permissible as long as the thermal conductivity of the reference object is linearly related to the temperature, which is the case for the temperature range investigated in this paper.

2.3. Heat flux sensor calibration

The calibration method presented in this paper is applied on a Peltier element, where the heat flux $\dot{q}$ is determined by measuring the thermo-electrical response U_{m} of the Peltier element [21]. For a reliable calibration, the heat flux sensor should be mounted in a way that is closest to the later operating conditions. Thereby the heat flow, which could pass the heat flow sensor, is also taken into account [22]. The ultimate goal of this investigation is to determine the inverse of the function

$$U_{\text{m}} = f(\dot{q}), \tag{7}$$

by calibration and to obtain the lowest possible uncertainties. The Peltier element calibrated in this investigation and built into the THFS described in section 2 is a commercially available one with a square area of side length $L_{\text{teg}} = 15\,\text{mm}$. The voltage U_{m} generated at the sensor terminals is in this case a direct consequence of the temperature difference between the two large planar sides. Thereby, the terminal voltage is linearly dependent on the temperature difference, which is defined by a proportionality factor also known as the Seebeck coefficient S [21]. Unfortunately, this coefficient itself is temperature dependent, which leads to:

$$U_{\text{m}} = S(\vartheta_{\text{teg}}) \cdot \Delta\vartheta_{\text{teg}}, \tag{8}$$

where ϑ_{teg} is the average temperature and $\Delta\vartheta_{\text{teg}}$ is the temperature difference between the two sides of the Peltier element, respectively. Further, the temperature difference $\Delta\vartheta_{\text{teg}}$ is caused by the heat flow through the sensor and can be expressed as:

$$\Delta\vartheta_{\text{teg}} = R_{\text{th-teg}} \cdot \dot{Q}_{\text{teg}} = R_{\text{th-teg}} \cdot \dot{q}_{\text{teg}} \cdot (L_{\text{teg}})^2. \tag{9}$$

Thereby, the Peltier element is assumed to be a thermally conductive solid with a lumped thermal resistance parameter $R_{\text{th-teg}}$. In this case equation (7) can be expressed in terms of the temperature dependent Seebeck coefficient $S(\vartheta_{\text{teg}})$ as:

$$U_{\text{m}} = S(\vartheta_{\text{teg}}) \cdot R_{\text{th-teg}} \cdot \dot{q}_{\text{teg}} \cdot (L_{\text{teg}})^2 \tag{10}$$

The heat flow $\dot{Q}_{\text{teg}}$ through the Peltier element is equal to the heat flow $\dot{Q}_{\text{ro}}$ in the reference body, which can also be expressed in terms of the temperature gradient according to:

$$\dot{Q}_{\text{teg}} = \dot{Q}_{\text{ro}} = -k \cdot \frac{\partial \vartheta}{\partial x} \cdot (L_{\text{ro}})^2 \tag{11}$$

where L_{ro} is the side length of the square cross-section of the reference object. This means that the applied calibration method is based on the determination of a temperature gradient within a reference object with known thermal properties. Therefore, the resulting heat flux $\dot{q}_{\text{teg}}$ through the Peltier element can be expressed as:

$$\dot{q}_{\text{teg}} = -k \cdot \frac{\partial \vartheta}{\partial x} \cdot \left(\frac{L_{\text{ro}}}{L_{\text{teg}}}\right)^2 = \frac{1}{S(\vartheta_{\text{teg}}) \cdot R_{\text{th-teg}} \cdot (L_{\text{teg}})^2} \cdot U_{\text{m}}. \tag{12}$$

The remaining unknown parameter in equation (12) is the Seebeck coefficient S and its temperature dependency. More precisely, the product $S(\vartheta_{\text{teg}}) \cdot R_{\text{th-teg}}$ has not yet been identified and must be determined by calibration experiments. Furthermore, in sensor technology the sensitivity

$$G(\vartheta_{\text{teg}}) = \frac{U_{\text{m}}(\vartheta_{\text{teg}})}{\dot{q}_{\text{teg}}} = S(\vartheta_{\text{teg}}) \cdot R_{\text{th-teg}} \cdot (L_{\text{teg}})^2, \tag{13}$$

is usually used to express the relationship between the sensor signal and the quantity to be measured [21]. For verification, both the sensor sensitivity and the Seebeck coefficient are compared with data from the literature. The standard operation procedure described hereafter was followed for all the experiments:

The THFS—or any other heat flux sensor—was placed with its front end aligned with the top face of the reference object. For reasons of improved thermal coupling a thin layer of heat transfer compound and a well-defined contact force was applied. The contact force was measured by means of a load cell and was chosen to be 20 N. A series of experiments was then carried out with a heat flux varying between -4500 and $12\,000\,\text{Wm}^{-2}$, which corresponds to a cooling power of $-1\,\text{W}$ or heating power of 2.5 W, respectively. The measurements of sensor terminal voltage and temperature distribution along the reference object were taken after steady state condition according to the definition in section 2.1 was reached. In order to achieve a wider sensor temperature range ϑ_{teg} for the calibration, the temperature set point of the cryostat—and therefore the surrounding temperature ϑ_{sur}—was varied between the different experiment series. For a number of cryostat temperature settings in the range of 14 °C–30 °C, the temperature dependent sensor sensitivity could be determined in the range of -10 °C to 75 °C.

3. Results and discussion

3.1. Linearity of temperature gradients

In this section the results of temperature gradient determination are discussed exemplary for an experiment with a heating power of 631.5 mW. As for all experiments, the heating power was kept constant until the temperature gradient had reached steady state, as defined in section 2.1. The measured data is shown in figure 2 and the corresponding values, including their respective standard uncertainties, can be found in table B1 of appendix B. By means of a linear regression, the slope and thus the temperature gradient as well as the associated uncertainty were determined, as being:

$$\frac{\partial \vartheta}{\partial x} = (-146.4 \pm 1.9)\,\mathrm{K\,m}^{-1}. \tag{14}$$

The residuals of the linear regression are below 10 mK as shown in figure 2(b), which is smaller by a factor of 5 compared to the combined standard uncertainty $u(\vartheta)$ of the temperature measurements. In addition, a coefficient of determination of $R^2 = 99.9991\%$ shows that the data set is very well approximated by the linear model.

This indicates that the thermal insulation along the sides of the reference object is sufficient and the heat losses via RTD signal lines are negligible. It can also be concluded that the heat flux $\dot{q}$ is almost constant within the reference object. For all performed experiments the derived uncertainties of the regression coefficients, i.e. of the temperature gradients, are in the range of 1.8–2.0 K m^{-1}.

For the sake of completeness, it should be mentioned that a thermal resistance between the heat flux sensor to be calibrated and the top surface of the reference object has no influence on the presented results, since the temperature gradient is not affected by a temperature drop across the contact surface.

3.2. Thermal conductivity

The reference object is made out of AISI 304 grade stainless steel, whose thermal conductivity is in principle available from the literature. However, the corresponding measurement uncertainties are often unknown or it is unclear how these values were determined. Therefore, the thermal conductivity of the material of the reference object is measured using the method described in section 2.2 and C. In addition, k is determined after the reference object was built into the calibration set-up. Thus the quality of the set-up design with regards to thermal properties can be evaluated, too. Figure 3(a) shows the dependency of the thermal conductivity k with respect to the average temperature ϑ_{m} of the reference object. The respective data including the measurement uncertainty are listed in table B2 in appendix B.

The linear regression with a coefficient of determination of $R^2 = 99.467\%$ in figure 3(a) indicates that the data set is very well described by the following linear model:

$$k = 9.819\,\frac{W}{m\,K} + 0.0173\,\frac{W}{m\,K^2} \cdot \vartheta_{\mathrm{m}}. \tag{15}$$

Table 2. Coefficients of the linear regression.

Polynomial coefficient	Fitted value
G_0	$(47.77 \pm 0.22)\,\mu\mathrm{V\,m}^2\,\mathrm{W}^{-1}$
G_1	$(0.141 \pm 0.011)\,\mu\mathrm{V\,m}^2\,(\mathrm{W\,K})^{-1}$

According to White [20] the thermal conductivity of AISI 304 stainless steel shows a linear relationship according to:

$$k = 9.687\,\frac{W}{m\,K} + 0.0173\,\frac{W}{m\,K^2} \cdot \vartheta_{\mathrm{m}}, \tag{16}$$

for temperatures above 0 °C. The found polynomial coefficients agree very well with the values found in the literature, which suggests that the method used for the analysis of the thermal conductivity is state of the art.

Nevertheless, with regard to the measurement uncertainty, it can be advantageous to determine the thermal conductivity ourselves. In figure 3(b) the residuals of the linear regression are shown together with the combined standard uncertainties of the calculated thermal conductivity k. As a worst case scenario the maximum uncertainty of 1.3% is taken into account for the error propagation of subsequent evaluation steps.

## 3.3. Calibration curve of the heat flux sensor

Figure 4 shows the calibration curve of the heat flux sensor mounted inside the THFS. As expected, the temperature dependence of the sensor sensitivity G is clearly visible, with an almost linear relationship up to a temperature of 35 °C according to equation (17) and the coefficients in table 2.

$$G = G_0 + G_1 \cdot \vartheta_{\mathrm{teg}}. \tag{17}$$

Compared to values from the literature, the achieved average uncertainty of $\pm 1.86\%$ is significantly lower. Haruyama [23] specified an uncertainty of $\pm 5\%$ for a Peltier element with 127 PN junctions and a size of 30 mm $\times$ 30 mm. Using a thermopile, Pullins and Diller [24] measured a heat flux caused by thermal radiation with an uncertainty of $\pm 7\%$. The most precise measurements found in the literature describe a method using a Gardon gauge to measure a heat flux in the range of 100 000 Wm^{-2} caused by thermal radiation [25]. The reported measurement uncertainty is between $+1.3\%$ and -0.6%. Furthermore, according to manufacturer data sheets commercially available heat flux sensors show uncertainties of not less than $\pm 3\%$ in the best case. The absolute sensitivity values differ considerably due to the different measuring principles. If a Peltier element is used as a heat flux sensor, the Seebeck coefficient of the electrothermal material can also be compared. In equation (13) it is assumed that the thermal resistance $R_{\mathrm{th\text{-}teg}}$ of the Peltier element is almost independent of temperature. The TEG used in this investigation has a lumped parameter of $R_{\mathrm{th\text{-}teg}} = 22.49\,\mathrm{K\,W}^{-1}$ within the relevant temperature range. Figure 4 shows the Seebeck coefficient and the sensor sensitivity as a function of the sensor average temperature ϑ_{teg}. Thereby, the average temperature is a linear extrapolation
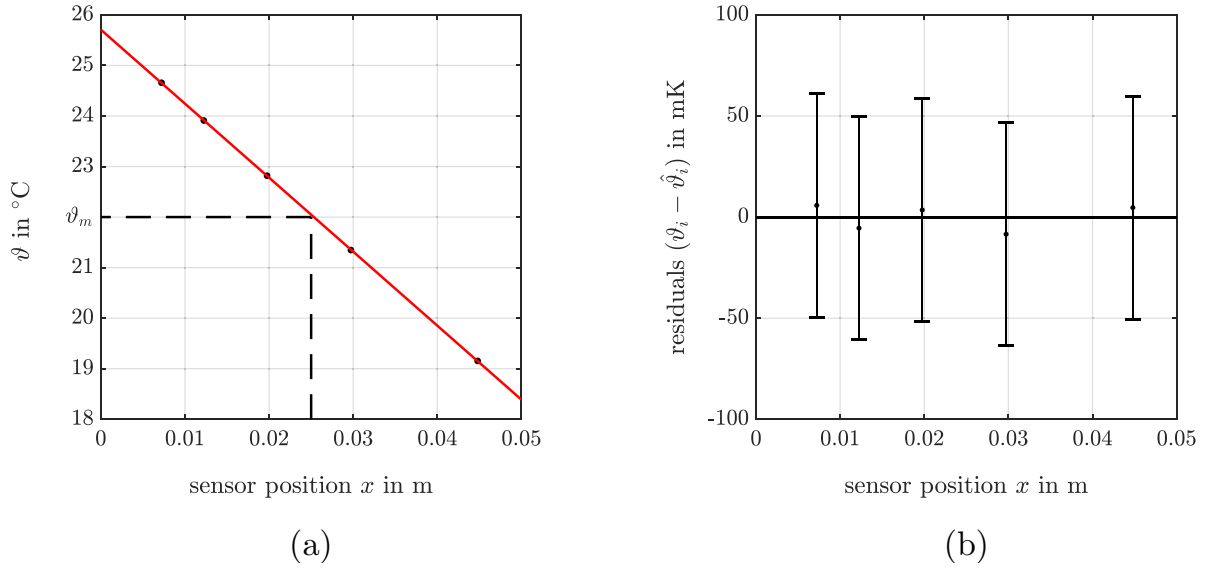
Figure 2. (a) Measured temperatures along the reference object (black dots) and the result of the linear regression (red line). The residuals (i.e. the vertical distance between a data point and the linear regression) shown in (b) are much smaller (below 10 mK) than the combined standard uncertainty of the temperature measurement itself.
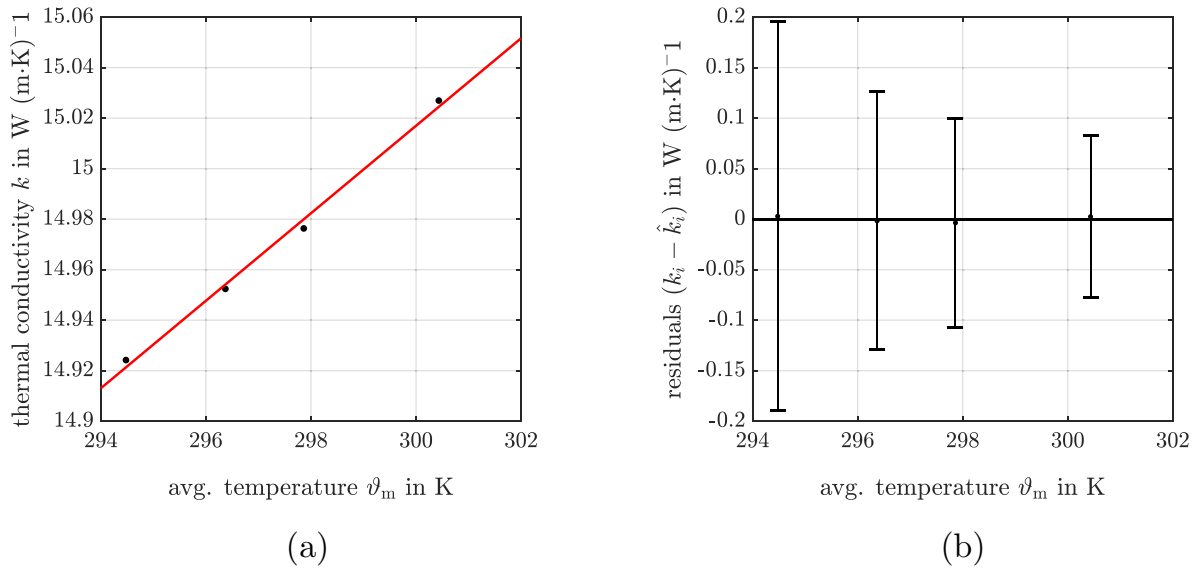
Figure 3. (a) Determined equivalent thermal conductivity k of the reference object plotted against the average temperature ϑ_m (black dots) and the result of the linear regression (red line). (b) The combined standard uncertainties of the thermal conductivity are significantly higher than the residuals of the linear regression.

from the measured temperature ϑ_{thfs} on one side of the TEG according to equation (18). The temperature difference across the TEG observed over all experiments is in the range of $-23°C$–$56\,°C$ and results from its relatively high thermal resistance $R_{th\text{-}teg}$.

$$\vartheta_{\text{teg}} = \vartheta_{\text{thfs}} + \frac{\dot{Q}_{\text{teg}} \cdot R_{\text{th}-\text{teg}}}{2} \qquad (18)$$

A linear behavior of the Seebeck coefficient is found up to about 35 °C, which decreases asymmetrically with increasing

temperature to a value of about $11\,\text{mV}\,\text{K}^{-1}$. Since this is a commercially available Peltier element, it can be assumed that it is composed of Bi_2Te_3 blocks, which are p- and n-doped accordingly [26]. The Seebeck coefficient of a single p/n junction of this kind of material at 20 °C is equal to $314\,\mu\,\text{V}\,\text{K}^{-1}$ [27]. The Peltier element used consists of 31 p/n junctions connected in series. Therefore a total Seebeck coefficient of $9.734\,\text{mW}\,\text{K}^{-1}$ can be expected. The measured value at 20 °C as shown in figure 4 is $9.999\,\text{mV}\,\text{K}^{-1}$, which deviates only $+2.7\%$ from the theoretical value.
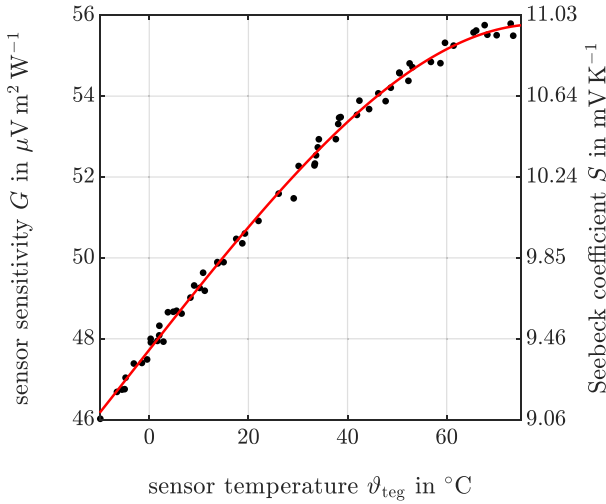
Figure 4. Calibration of heat flux sensors in terms of sensor sensitivity *G* and its Seebeck coefficient *S*.

4. Conclusions

An accurate heat flux sensor calibration presumes precise determination of the amount of heat transferred per unit of time through the sensor. The presented calibration set-up design fulfills the requirements for adequate heat flux measurement: heat losses through the insulation as well as along any signal or power lines can be neglected and hence do not noticeable influence the linearity of the detected temperature gradient inside the actual reference object. In addition, it is shown that overall error propagation leads to a significantly better level of measurement uncertainty by determining the thermal conductivity of the reference object material already mounted in the set-up in advance. In this way, uncertainties caused by the design of the set-up are included in the equivalent thermal conductivity value identified and no additional inaccuracies induced by a separate calibration step need to be considered subsequently. Furthermore, the determined temperature dependence of the thermal conductivity of the reference object material is so close to the data published for AISI 304 that it can be taken as proof that the set-up procedure described here are consistent with state-of-the-art thermal analysis methods. As a result of the heat flux sensor calibration, the sensor sensitivity *G* is determined. In addition, if a Peltier element is used as TEG its Seebeck coefficient *S* is also identified. Up to a temperature of 35 °C, the temperature dependency of these two calibration factors are well approximated by a linear relation. The total uncertainties of measurement for these values are ±1.86%, which is verifiably below published results. The absolute value of the determined Seebeck coefficient for the examined Peltier element with 31 p/n junctions at a temperature of 20 °C is only 2.7% above the published theoretical values for the same material.

Acknowledgments

Funding

Appendix A. Formulas to calculate the uncertainty of the coefficients of a linear regression

The aim of the linear regression is to find the coefficients β_1 and β_0 of a linear model so that the function

$$y = \beta_0 + \beta_1 \cdot x \tag{A1}$$

approximates the data points as well as possible. The equations (A1)–(A8) are taken from [15] and are used to calculate the coefficients β_0 and β_1, as well as the standard uncertainty $u(\beta_1)$. The mean values $\bar{x}$ and $\bar{y}$ of the two data sets (x_i and y_i) consisting of N data points are given by:

$$\bar{x} = \frac{1}{n}\sum_{i=1}^{n} x_i \qquad \text{and} \qquad \bar{y} = \frac{1}{n}\sum_{i=1}^{n} y_i \tag{A2}$$

From this, the following sums can be defined for later use:

$$S_{xx} \equiv \sum_{i=1}^{n}(x_i - \bar{x})^2, \qquad S_{yy} \equiv \sum_{i=1}^{n}(y_i - \bar{y})^2, \tag{A3}$$

$$S_{xy} \equiv \sum_{i=1}^{n}(x_i - \bar{x})(y_i - \bar{y}). \tag{A4}$$

Those sums are used to calculate the slope and the constant term of the linear model according to:

$$\beta_1 = sign(S_{xy}) \cdot \sqrt{\frac{S_{yy}}{S_{xx}}} \tag{A5}$$

$$\beta_0 = \bar{y} - \beta_1 \cdot \bar{x} \tag{A6}$$

The uncertainty of the slope β_1 can be expressed as:

$$u^2(\beta_1) = \sum_{i=1}^{n}(c_{xi} \cdot u(x_i))^2 + \sum_{i=1}^{n}(c_{yi} \cdot u(y_i))^2 \tag{A7}$$

where $u(x_i)$ and $u(y_i)$ are the standard uncertainties of the underlying data sets, respectively. The coefficients c_{xi} and c_{yi} are expressions for the respective partial derivatives $\partial\beta_1/\partial x_i$ and $\partial\beta_1/\partial y_i$ used in the law of error propagation and can be calculated as:

$$c_{xi} = \frac{\beta_1(x_i - \bar{x})}{S_{xx}} \qquad \text{and} \qquad c_{yi} = \frac{\beta_1(y_i - \bar{y})}{S_{yy}} \tag{A8}$$

Table B1. Data sets x_i and ϑ_i including the standard uncertainties used for the linear regression shown in figure 2(a) of section 3.1.

Sensor position x	Temperature ϑ
(7.218 ± 0.058) mm	$(24.657 \pm 0.055)\,°C$
(12.240 ± 0.058) mm	$(23.910 \pm 0.055)\,°C$
(19.761 ± 0.058) mm	$(22.818 \pm 0.055)\,°C$
(29.728 ± 0.058) mm	$(21.347 \pm 0.055)\,°C$
(44.795 ± 0.058) mm	$(19.154 \pm 0.055)\,°C$

Table B2. Data sets $\vartheta_{m,i}$ and k_i including the standard uncertainties used for the linear regression shown in figure 3(a) of section 3.2.

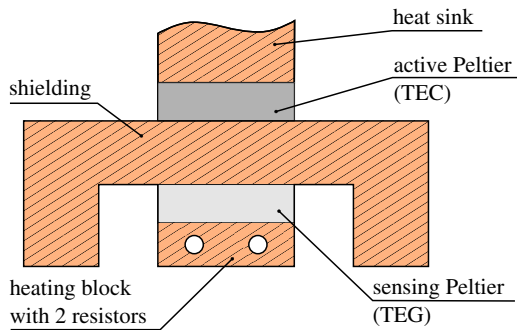| Avg. temperature ϑ_m	Thermal conductivity k
(294.479 ± 0.055) K	$(14.92 \pm 0.19)\,W\,(m\,K)^{-1}$
(296.371 ± 0.055) K	$(14.95 \pm 0.13)\,W\,(m\,K)^{-1}$
(297.863 ± 0.056) K	$(14.98 \pm 0.10)\,W\,(m\,K)^{-1}$
(300.433 ± 0.056) K	$(15.027 \pm 0.080)\,W\,(m\,K)^{-1}$

Appendix B. Data sets with uncertainties

Appendix C. Single-sided guarded hot plate method as used for the heat flux sensor calibrator

To determine the equivalent thermal conductivity of the reference object, a precisely defined heat flow has to be introduced into the reference object. Therefore, a heating unit surrounded by a protection heating device was designed. This is schematically depicted in figure C1(a) and shown from the underside in figure C1(b). Two ohmic resistor heater installed in the inner copper block were used as a heat source. This copper block is in direct contact with the top surface of the cuboid reference object. The main challenge is to guarantee that the heat generated by the electrical power of the heaters is guided into the reference object without any heat loss. Any heat bypassing the reference object will lead to additional inaccuracies in the equivalent thermal conductivity value of the reference object used and hence to an incorrect calibration. To prevent this, the design principles of a single-sided guarded hot plate apparatus [19] were applied. The idea behind this, is to prevent heat flow by heating the surroundings to the same temperature as the surface temperature of the reference object (i.e. no temperature gradient, no heat flux). As can be seen in figure C1, this kind of protective heating is realized by a copper cap, which is placed on top of the heating block. With the help of a separate electrical heating circuit the copper cap can be heated independently. To detect the temperature difference between the heating block and the protective copper cap, a TEG is used between the two. The output voltage of the TEG is a direct measure of the temperature gradient through it, whereby the voltage drops to zero when there is no temperature difference between top and bottom surface. That means that the heating of the copper cap has to be controlled so that the voltage of TEG element is equal to zero throughout the entire experiment. Only under these conditions can it be assumed with a high probability that the heat flow rate introduced into the ashlar-formed reference

Table B3. Data sets $\vartheta_{teg,i}$ and G_i used for the 3rd order polynomial fit shown in figure 4 of section 3.3.

Temperature ϑ_{teg}	Sensitivity G
$(-9.9 \pm 1.4)\,°C$	$(46.02 \pm 0.86)\,\mu V^2\,W^{-1}$
$(-6.5 \pm 1.4)\,°C$	$(46.69 \pm 0.87)\,\mu V^2\,W^{-1}$
$(-5.5 \pm 1.4)\,°C$	$(46.74 \pm 0.89)\,\mu V^2\,W^{-1}$
$(-5.0 \pm 1.4)\,°C$	$(46.75 \pm 0.92)\,\mu V^2\,W^{-1}$
$(-4.8 \pm 1.4)\,°C$	$(47.04 \pm 0.87)\,\mu V^2\,W^{-1}$
$(-3.1 \pm 1.4)\,°C$	$(47.39 \pm 0.88)\,\mu V^2\,W^{-1}$
$(-1.5 \pm 1.4)\,°C$	$(47.40 \pm 0.93)\,\mu V^2\,W^{-1}$
$(-0.4 \pm 1.4)\,°C$	$(47.49 \pm 0.98)\,\mu V^2\,W^{-1}$
$(0.3 \pm 1.4)\,°C$	$(48.00 \pm 0.88)\,\mu V^2\,W^{-1}$
$(0.3 \pm 1.4)\,°C$	$(47.91 \pm 0.90)\,\mu V^2\,W^{-1}$
$(1.6 \pm 1.4)\,°C$	$(47.95 \pm 0.95)\,\mu V^2\,W^{-1}$
$(2.0 \pm 1.4)\,°C$	$(48.08 \pm 0.94)\,\mu V^2\,W^{-1}$
$(2.0 \pm 1.4)\,°C$	$(48.32 \pm 0.89)\,\mu V^2\,W^{-1}$
$(2.9 \pm 1.4)\,°C$	$(47.9 \pm 1.2)\,\mu V^2\,W^{-1}$
$(3.8 \pm 1.4)\,°C$	$(48.66 \pm 0.89)\,\mu V^2\,W^{-1}$
$(4.8 \pm 1.4)\,°C$	$(48.67 \pm 0.92)\,\mu V^2\,W^{-1}$
$(5.5 \pm 1.4)\,°C$	$(48.69 \pm 0.94)\,\mu V^2\,W^{-1}$
$(6.5 \pm 1.4)\,°C$	$(48.6 \pm 1.2)\,\mu V^2\,W^{-1}$
$(8.3 \pm 1.4)\,°C$	$(49.0 \pm 1.0)\,\mu V^2\,W^{-1}$
$(9.1 \pm 1.4)\,°C$	$(49.32 \pm 0.95)\,\mu V^2\,W^{-1}$
$(10.2 \pm 1.4)\,°C$	$(49.3 \pm 1.2)\,\mu V^2\,W^{-1}$
$(10.9 \pm 1.4)\,°C$	$(49.63 \pm 0.96)\,\mu V^2\,W^{-1}$
$(11.2 \pm 1.4)\,°C$	$(49.2 \pm 2.1)\,\mu V^2\,W^{-1}$
$(13.7 \pm 1.4)\,°C$	$(49.9 \pm 1.1)\,\mu V^2\,W^{-1}$
$(13.8 \pm 1.4)\,°C$	$(49.9 \pm 1.2)\,\mu V^2\,W^{-1}$
$(15.0 \pm 1.4)\,°C$	$(49.9 \pm 2.1)\,\mu V^2\,W^{-1}$
$(17.5 \pm 1.4)\,°C$	$(50.5 \pm 1.2)\,\mu V^2\,W^{-1}$
$(18.8 \pm 1.4)\,°C$	$(50.4 \pm 2.1)\,\mu V^2\,W^{-1}$
$(19.3 \pm 1.4)\,°C$	$(50.6 \pm 3.5)\,\mu V^2\,W^{-1}$
$(22.0 \pm 1.4)\,°C$	$(50.9 \pm 1.6)\,\mu V^2\,W^{-1}$
$(26.1 \pm 1.4)\,°C$	$(51.6 \pm 1.6)\,\mu V^2\,W^{-1}$
$(29.1 \pm 1.4)\,°C$	$(51.5 \pm 3.7)\,\mu V^2\,W^{-1}$
$(30.1 \pm 1.4)\,°C$	$(52.3 \pm 1.6)\,\mu V^2\,W^{-1}$
$(33.3 \pm 1.4)\,°C$	$(52.3 \pm 1.0)\,\mu V^2\,W^{-1}$
$(33.4 \pm 1.4)\,°C$	$(52.3 \pm 1.1)\,\mu V^2\,W^{-1}$
$(33.6 \pm 1.4)\,°C$	$(52.5 \pm 1.2)\,\mu V^2\,W^{-1}$
$(34.0 \pm 1.4)\,°C$	$(52.7 \pm 1.4)\,\mu V^2\,W^{-1}$
$(34.2 \pm 1.4)\,°C$	$(52.9 \pm 1.6)\,\mu V^2\,W^{-1}$
$(37.6 \pm 1.4)\,°C$	$(52.9 \pm 1.0)\,\mu V^2\,W^{-1}$
$(38.1 \pm 1.4)\,°C$	$(53.3 \pm 1.4)\,\mu V^2\,W^{-1}$
$(38.3 \pm 1.4)\,°C$	$(53.5 \pm 1.6)\,\mu V^2\,W^{-1}$
$(38.6 \pm 1.4)\,°C$	$(53.5 \pm 1.9)\,\mu V^2\,W^{-1}$
$(41.9 \pm 1.4)\,°C$	$(53.5 \pm 1.1)\,\mu V^2\,W^{-1}$
$(42.4 \pm 1.4)\,°C$	$(53.9 \pm 1.6)\,\mu V^2\,W^{-1}$
$(44.3 \pm 1.4)\,°C$	$(53.7 \pm 1.0)\,\mu V^2\,W^{-1}$
$(46.2 \pm 1.4)\,°C$	$(54.1 \pm 1.1)\,\mu V^2\,W^{-1}$
$(47.7 \pm 1.4)\,°C$	$(53.88 \pm 0.96)\,\mu V^2\,W^{-1}$
$(48.7 \pm 1.4)\,°C$	$(54.2 \pm 1.0)\,\mu V^2\,W^{-1}$
$(50.4 \pm 1.4)\,°C$	$(54.6 \pm 1.1)\,\mu V^2\,W^{-1}$
$(50.5 \pm 1.4)\,°C$	$(54.6 \pm 1.1)\,\mu V^2\,W^{-1}$
$(52.3 \pm 1.4)\,°C$	$(54.38 \pm 0.96)\,\mu V^2\,W^{-1}$
$(52.5 \pm 1.4)\,°C$	$(54.8 \pm 1.1)\,\mu V^2\,W^{-1}$
$(53.1 \pm 1.4)\,°C$	$(54.7 \pm 1.0)\,\mu V^2\,W^{-1}$
$(56.8 \pm 1.4)\,°C$	$(54.85 \pm 0.97)\,\mu V^2\,W^{-1}$

(Continued)

(a) Schematic cross section.
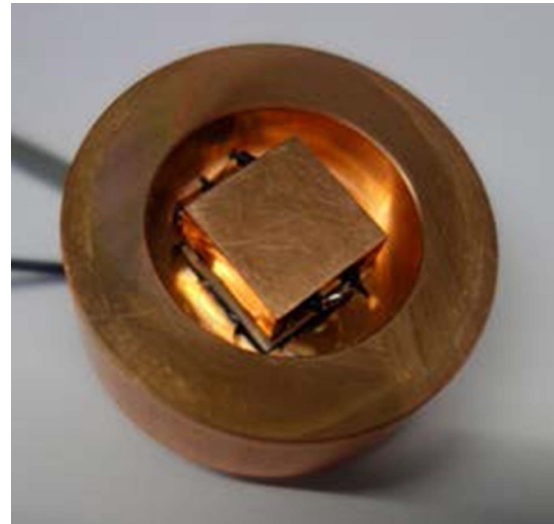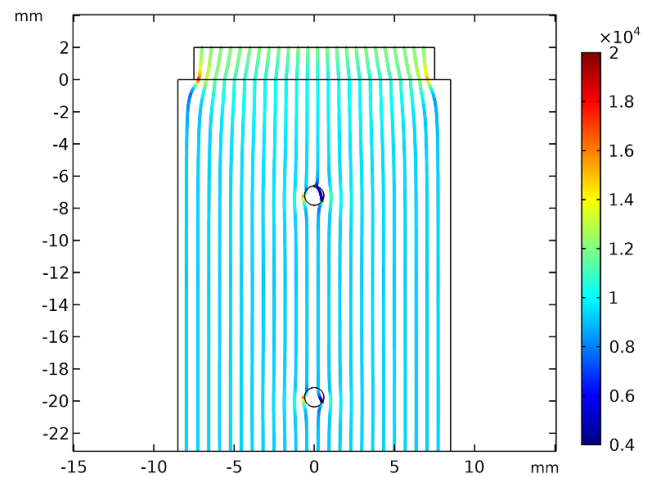
(b) Photograph of the inside.

Figure C1. Heating unit for determining the thermal conductivity of the ashlar-formed stainless steel test section with a protective heating cap.

Table B3. (Continued.)

Temperature ϑ_{teg}	Sensitivity G
$(58.7 \pm 1.4)\,^\circ\mathrm{C}$	$(54.81 \pm 0.95)\,\mu\mathrm{V}^2\,\mathrm{W}^{-1}$
$(59.7 \pm 1.4)\,^\circ\mathrm{C}$	$(55.3 \pm 1.0)\,\mu\mathrm{V}^2\,\mathrm{W}^{-1}$
$(61.4 \pm 1.4)\,^\circ\mathrm{C}$	$(55.25 \pm 0.98)\,\mu\mathrm{V}^2\,\mathrm{W}^{-1}$
$(65.4 \pm 1.4)\,^\circ\mathrm{C}$	$(55.57 \pm 0.99)\,\mu\mathrm{V}^2\,\mathrm{W}^{-1}$
$(66.0 \pm 1.4)\,^\circ\mathrm{C}$	$(55.62 \pm 0.98)\,\mu\mathrm{V}^2\,\mathrm{W}^{-1}$
$(67.7 \pm 1.4)\,^\circ\mathrm{C}$	$(55.76 \pm 0.99)\,\mu\mathrm{V}^2\,\mathrm{W}^{-1}$
$(68.2 \pm 1.4)\,^\circ\mathrm{C}$	$(55.52 \pm 0.96)\,\mu\mathrm{V}^2\,\mathrm{W}^{-1}$
$(70.1 \pm 1.4)\,^\circ\mathrm{C}$	$(55.51 \pm 0.95)\,\mu\mathrm{V}^2\,\mathrm{W}^{-1}$
$(72.9 \pm 1.4)\,^\circ\mathrm{C}$	$(55.79 \pm 0.97)\,\mu\mathrm{V}^2\,\mathrm{W}^{-1}$
$(73.4 \pm 1.4)\,^\circ\mathrm{C}$	$(55.49 \pm 0.95)\,\mu\mathrm{V}^2\,\mathrm{W}^{-1}$

Figure C2. Results of the FEA in the upper portion of the reference object including the interface to the smaller THFS copper plate. The color coded streamlines represent the heat flux in $\mathrm{W\,m}^{-2}$.

object is equal to the electrical power dissipated inside the resistor heaters. Unfortunately, some heat paths remain allowing heat to bypass the reference object.

One heat path is through the insulation between the heating block and the copper cap. FEM simulation demonstrated that this amount of heat is less than 0.04% of the heating power and hence insignificant. A second heat path to bypass the reference object is via the power lines of the ohmic resistor heaters. To prevent this, the wires are mounted in a meander with thermal contact to the protective heating cap. Thus, the wires will have nearly the same temperature as the copper cap and the heating block. Due to a lack of temperature gradients according to equation (1) there will be no heat transfer. In addition it should be noted, that the heating block was designed to have the same physical dimension as the actual sensors which will be calibrated, i.e. an edge length of 15 mm. The difference of the cross-sectional areas of the sensor and the reference object will introduce a non-unidirectional heat flow in the top section of the reference object. Also, the small difference in the thermal conductivity of the RTD material and the stainless steel in combination with the possibly non-uniform

contact of the RTD probe, are disrupting the uni-axial heat flow. In order to quantify this influences a 3D finite element analysis (FEA) has been performed. In figure C2 a color-coded stream line plot of the heat flux in $\mathrm{W\,m}^{-2}$ of the upper part of the reference object is shown. The FEA showed that the combination of all the above mentioned effects would introduce an error when the heat flow was calculated by the measured temperature gradient and the nominal thermal conductivity of the reference material (i.e. stainless steel). The FEA analysis shows that this error of the calculated heat flux could be up to 1%. However, with the methodology described in this paper an equivalent thermal conductivity of the reference object including all the mentioned imperfections is determined as described in section 2.2. The heat flux sensor calibration is than performed with the exact same reference object,

hence the equivalent thermal conductivity can be used to accurately calculate the existing heat flux within the reference object.

ORCID iDs

G Rizzo ⬡ https://orcid.org/0000-0002-2348-9764
R Christen ⬡ https://orcid.org/0000-0002-5363-1426

References

[1] Sarge S M, Höhne Gunther W H and Hemminger W (ed) 2014 *Calorimetry: Fundamentals, Instrumentation and Applications* (Weinheim: Wiley-VCH) p 304

[2] Murashko K A, Mityakov A V, Mityakov V Y, Sapozhnikov S Z, Jokiniemi J and Pyrhönen J 2016 Determination of the entropy change profile of a cylindrical lithium-ion battery by heat flux measurements *J. Power Sources* **330** 61–9

[3] Aiello L, Kovachev G, Brunnsteiner B, Schwab M, Gstrein G, Sinz W and Ellersdorfer C 2020 In situ measurement of orthotropic thermal conductivity on commercial pouch lithium-ion batteries with thermoelectric device *Batteries* **6** 1–17

[4] Childs P R N, Greenwood J R and Long C A 1999 Heat flux measurement techniques *Proc. Inst. Mech. Eng.* C **213** 655–77

[5] Zhang Y and Jahns T 2014 Power electronics loss measurement using new heat flux sensor based on thermoelectric device with active control *IEEE Trans. Ind. Appl.* **50** 4098–106

[6] Robador A, LaRowe D E, Finkel S E, Amend J P and Nealson K H 2018 Changes in microbial energy metabolism measured by nanocalorimetry during growth phase transitions *Front. Microbiol.* **9** 1–7

[7] Krenger R, Lehnert T and Gijs M A M 2018 Dynamic microfluidic nanocalorimetry system for measuring Caenorhabditis elegans metabolic heat *Lab Chip* **18** 1641–51

[8] Gunes M, Parlak M and Ozenbas M 2014 An instrument for the high temperature measurement of the Seebeck coefficient and electrical resistivity *Meas. Sci. Technol.* **25** 055901

[9] Fu X *et al* 2020 High-temperature heat flux sensor based on tungsten-rhenium thin-film thermocouple *IEEE Sens. J.* **20** 10444–52

[10] Burkov A T, Heinrich A, Konstantinov P P, Nakama T and Yagasaki K 2001 Experimental set-up for thermopower and resistivity measurements at 100–1300 K *Meas. Sci. Technol.* **12** 304

[11] Sharma P K, Sharma V K, Senguttuvan T D and Chaudhary S 2020 Design, fabrication and calibration of low cost thermopower measurement set up in low- to mid-temperature range *Measurement* **150** 107054

[12] Hohmann M, Schalles M and Fröhlich T 2016 Calibration of heat flux sensors for the detection of small heat fluxes *Tech. Mess. tm* **83** 393–401

[13] Logan D L 2017 *A First Course in the Finite Element Method* 6th edn (Australia: Cengage Learning) p 955

[14] Bergman T L, Lavine A and Incropera F P 2017 *Fundamentals of Heat and Mass Transfer* 8th edn (Hoboken, NJ: Wiley) p 992

[15] Matus M 2005 Coefficients and adjustment calculations: measurement uncertainty under GUM. Part 1: best fit straight lines *Tech. Mess. tm* **72** 584–91

[16] Christen R, Rizzo G, Gadola A and Stöck M 2017 Test method for thermal characterization of Li-ion cells and verification of cooling concepts *Batteries* **3** 3

[17] Leephakpreeda T 2012 Applications of thermoelectric modules on heat flow detection *ISA Trans.* **51** 345–50

[18] Joint Committee for Guides in Metrology 2008 JCGM 100:2008 Evaluation of measurement data—guide to the expression of uncertainty in measurement: GUM 1995 with minor corrections Technical report (https://www.bipm.org/utils/common/documents/jcgm/JCGM_100_2008_E.pdf)

[19] Terzic M, Milosevic N, Stepanic N and Petricevic S 2016 Development of a single-sided guarded hot plate apparatus for thermal conductivity measurements *Therm. Sci.* **20** 321–9

[20] White G K Thermal conductivity of pure metals and alloys. Volume 15c: 'thermal conductivity of pure metals and alloys' in Springer Materials (https://doi.org/10.1007/10031435_10)

[21] Pineda D D, Pineda D D, Rezaniakolaei A, Brand O, Fedder G K, Hierold C, Korvink J G and Tabata O (ed) 2017 *Thermoelectric Energy Conversion: Basic Concepts and Device Applications (Advanced Micro & Nanosystems)* 1st edn (Weinheim: Wiley-VCH) p 336

[22] Göpel W, Hesse J, Ed Zemel J N, Ed Grandke T, Ko W H, Boll R, Ricolfi T, Scholz J and Wagner E 2008 *Sensors: A Comprehensive Survey* (Weinheim: Wiley-VCH) p 656

[23] Haruyama T 2001 Performance of peltier elements as a cryogenic heat flux sensor at temperatures down to 60 k *Cyrogenics* **41** 335–9

[24] Pullins C A and Diller T E 2010 In situ high temperature heat flux sensor calibration *Int. J. Heat Mass Transfer* **53** 3429–38

[25] Ballestrín J, Estrada C A, Rodríguez-Alonso M, Pérez-Rábago C, Langley L W and Barnes A 2006 Heat flux sensors: calorimeters or radiometers? *Sol. Energy* **80** 1314–20

[26] Riffat S B and Xiaoli M 2003 Thermoelectrics: a review of present and potential applications *Appl. Therm. Eng.* **23** 913–35

[27] Han Mi-K, Jin Y, Lee D-H and Kim S-J 2017 Thermoelectric properties of Bi_2Te_3: CuI and the effect of its doping with Pb atoms *Materials (Basel, Switzerland)* **10** 1235